PERGAMON

International Journal of Rock Mechanics and Mining Sciences 37 (2000) 337–356

International Journal of
Rock Mechanics
and Mining Sciences

www.elsevier.com/locate/ijrmms

A field study for understanding thermally driven coupled processes in partially saturated fractured welded tuff

Y.W. Tsang*

Earth Sciences Division, Ernest Orlando Lawrence Berkeley National Laboratory, MS90-1116, 1 Cyclotron Road, Berkeley, CA 94720, USA

Accepted 7 October 1999

Abstract

As part of a multi-laboratory team, we are carrying out two in situ thermal tests — the single Heater Test and Drift Scale Test, in an underground facility at Yucca Mountain, Nevada, USA, the proposed site for a high-level nuclear waste repository. Our objective in these tests is to gain a more in-depth understanding of the coupled thermal–hydrological–mechanical–chemical processes likely to exist in the fractured rock mass around a geological repository. These coupled processes are monitored continuously by numerous sensors emplaced in boreholes, while cross-hole radar tomography, neutron logging, electrical resistivity tomography, and interference air-permeability tests all serve to measure moisture change in the rock mass. Thermal–hydrological processes for both tests have been simulated (using a 3-D numerical model) and compared to the extensive data set.

In this paper, we present examples to illustrate how an iterative approach requiring close integration of modeling and measurements enables us to track the complex coupled processes we seek to understand. The main manifestation of coupled thermal-hydrological processes is in the time evolution of the drying and condensation zones. Good agreement exists between model predictions and measurements, specifically the decrease in air-permeability values within zones of increased liquid saturation in the fractures and the increase of radar velocity in cross-hole radar survey in zones of decreased matrix liquid saturation. A heat-pipe signature in the temperature data arising from liquid–vapor counter-flow occurs in both the measurements and simulated results. The good agreement between predictions from the numerical simulations and measurements in the thermal tests indicates that our basic understanding of the thermal-hydrological processes in a potential repository at Yucca Mountain is sound. However, detailed behavior is impacted by site-specific heterogeneity, in the form of discrete fractures that are not likely to be predictable a priori. One emphasis of the on-going Drift Scale Test is to build on the present understanding and to assess the impact of heterogeneity to the repository performance.

Keywords: Thermal; Hydrological; Fractured rock; Field test; Yucca Mountain

1. Introduction

Heat is an important issue in the performance of a nuclear waste repository. Heat generated from the decay of nuclear waste affects the waste package environment, whose characteristics control the corrosion of waste canisters and the mobilization rate of radionuclides. Heat also influences the possible migration of radionuclides away from the potential repository into the environment. The densely fractured welded-tuff formation at Yucca Mountain, Nevada, is the proposed site for a national high-level nuclear waste repository. In order to assess the impact of heat on the performance of the repository, two in situ thermal tests, the Single Heater Test and Drift Scale Test, are being carried out in an underground facility — the Exploratory Studies Facility (ESF).

The primary objective of the ESF Thermal Tests is to develop a better understanding of the coupled ther-

* Corresponding author. Tel.: +1-510-486-7047; fax: +1-510-486-6115.

E-mail address: ytsang@lbl.gov (Y.W. Tsang).

1365-1609/00/$ - see front matter
PII: S1365-1609(99)00110-0

mal, mechanical, hydrological, and chemical processes likely to exist in the rock mass surrounding the potential geological repository at Yucca Mountain. In our attempt to sort out the complex, multiple-coupled processes in this heterogeneous, fractured natural environment, we have implemented a close integration between measurements and modeling.

Measurements in the in situ thermal tests include pre-heat laboratory and field characterization of the thermal test block, passive monitoring and active testing during the heating and cooling phases of the thermal tests, and post-cooling laboratory and field characterization activities similar to those conducted before the activation of heat. Pre-test laboratory characterization includes measurement of thermal properties, hydrological properties, mechanical properties, mineral–petrology studies, and pore-water chemical and isotopic analysis from thermal test block rock cores [1,2]. Pre-heat field characterization of the thermal test block involves rock-mass classification, fracture mapping, video logging of the boreholes, and air-permeability testing. The pre-heat data provide input to the numerical model that predicts the performance of the thermal tests. Measurements taken during the heating and cooling phases of the thermal tests in turn refine and calibrate the predictive model, thus reducing parameter and conceptual model uncertainty. Post-cooling laboratory and field measurements affirm the coupled processes that have left their imprint in the rock mass. For example, locations of drying and condensing zones resulting from thermal–hydrological coupled processes may be determined from laboratory matrix liquid-saturation measurements taken from cores drilled post-test. Alternatively, thermal–mechanical processes such as thermally induced stiffening of the fractured welded tuff may be uncovered by laboratory compressive strength measurements for core drilled post-test. Finally, post-heat, cross-hole air-permeability tests in the test block may detect effects of thermal–hydrological–mechanical coupled processes such as generation of new fractures and opening of existing fractures.

2. Thermal test setting and previous work

Both the Single Heater Test (SHT) and the Drift Scale Test (DST) are conducted in one of the side alcoves at the proposed repository horizon in the ESF. The ESF consists of an 8-km long tunnel with seven side alcoves for conducting underground experiments. The 8-m-diameter tunnel passes through the different stratigraphic units of Yucca Mountain: the alluvium at the surface, down through the Tiva Canyon welded and the Paintbrush nonwelded tuffs, and reaching the proposed repository horizon of Topopah Spring welded tuff, hundreds of meters above the water table.

At the time of writing, all testing activities and analyses have been completed for the SHT, whereas the DST is in its first year of heating for a planned eight-year-long experiment. The SHT consists of a 5-m-long heating element, at a nominal 4 kW, emplaced horizontally among 30 instrumental boreholes spanning a rock block of approximately $13 \times 10 \times 13$ m (Fig. 1). The heater in the SHT was activated on 26 August 1996. The heating phase of the SHT lasted nine months until 28 May 1997. The cooling phase of the SHT continued until 5 January 1998, at which time post-cooling field characterization activities began. The SHT was successful with respect to good quality of data and agreement with predictions from numerical models. Furthermore, the SHT, as the first of the two large-scale underground tests, provided insights in testing method, data acquisition logistics, data interpretation, and modeling strategies. These insights are being applied to the much larger-scale and longer-duration DST.

Heating for the DST was initiated on 3 December 1997 at 187 kW, for a planned heating period of four years. The DST centers around the 47.5-m-long Heated Drift, complemented by the Connecting Drift to the east and the Observation Drift that runs parallel to the Heated Drift (Fig. 2a) in an approximate E-W orientation. Heating is provided by nine canister heaters within the Heated Drift and 50 11-m-long wing heaters (Fig. 2b), flanking the north and south sides of the Heated Drift. The configuration of the heaters and their heating rate was designed to heat up a large volume of rock mass in a reasonably short period of time (a few years) to induce the thermal–hydrological conditions that would be reached only after 50 to 100 years of waste emplacement in the repository. Furthermore, the wing heaters would simulate the effect of heat from adjacent waste emplacement drifts in a repository, where the present design calls for waste emplacement drifts with center-to-center spacing of 28 m.

Close to 100 instrumented boreholes in the DST test block have been installed with thousands of sensors to monitor thermal, mechanical, hydrological, and chemical processes, with passive monitoring data recorded on at least an hourly basis. These boreholes are color coded according to their functions in Fig. 2a. To monitor the temperature evolution, temperature sensors are placed (at approximately 0.3 m space interval) in radial arrays of 20-m-long boreholes emanating from the Heated Drift, as well as in longitudinal boreholes parallel to and extending over the entire length of the Heated Drift. Multi-point borehole extensometers for monitoring the mechanical displacement in the rock mass were installed in boreholes configured similar to the thermal boreholes. Most boreholes

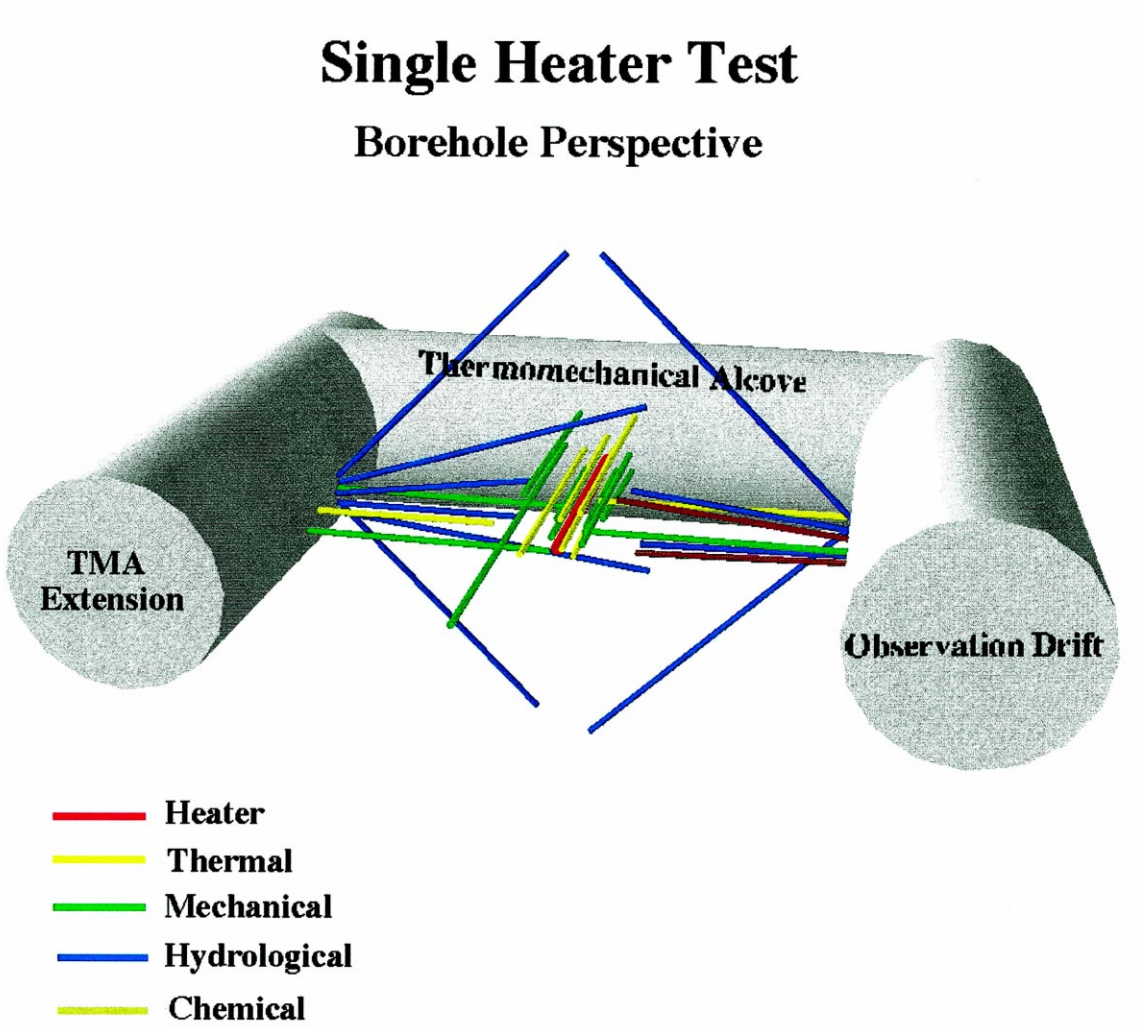

Fig. 1. Schematic of borehole layout for the Single Heater Test (3-D perspective).

labeled as hydrological and chemical do not emanate from the Heated Drift; rather, they originate from the Observation Drift. These are clusters of 40-m-long boreholes forming vertical fans that bracket the Heated Drift and the wing heaters. Humidity, temperature, and pressure sensors were installed in some of these holes to provide passive monitoring data. However, these boreholes are primarily used for periodic active testing to monitor the time evolution and spatial distribution of drying and condensation zones in the test block, and to collect water and gas samples for chemical and isotopic analysis.

With respect to scale, heater power, duration of test, and number of coupled processes studied, the DST is unprecedented. Most previous thermal tests were conducted in formation below the water table in the saturated zone, and emphasized the thermal–mechanical processes. In the late 1970s, in situ heater experiments were performed in drifts excavated in saturated granite rock adjacent to an abandoned iron ore mine in Stripa, Sweden. Some selected papers describing these thermal tests at Stripa are found in Cook and Hood [3], Cook and Witherspoon [4], Chan and Cook [5], Witherspoon et al. [6], and Dubois et al. [7]. The experiments operated up to a power of 6.1 kW and lasted for 4.5 years. They were designed to assess the near-field thermal–mechanical response of the rock near the heater canisters in the short term and under simulated conditions of rock temperature in the long term. The Basalt Waste Isolation Project (BWIP) conducted two in situ canister-scale heater experiments. Gregory and Kim [8] reported on the rock-mass response to thermal loading and the onset of thermally induced emplacement borehole instability. The issue of the stability of boreholes for potential in-floor borehole emplacement of nuclear waste was also examined by Martino and Read [9] in a series

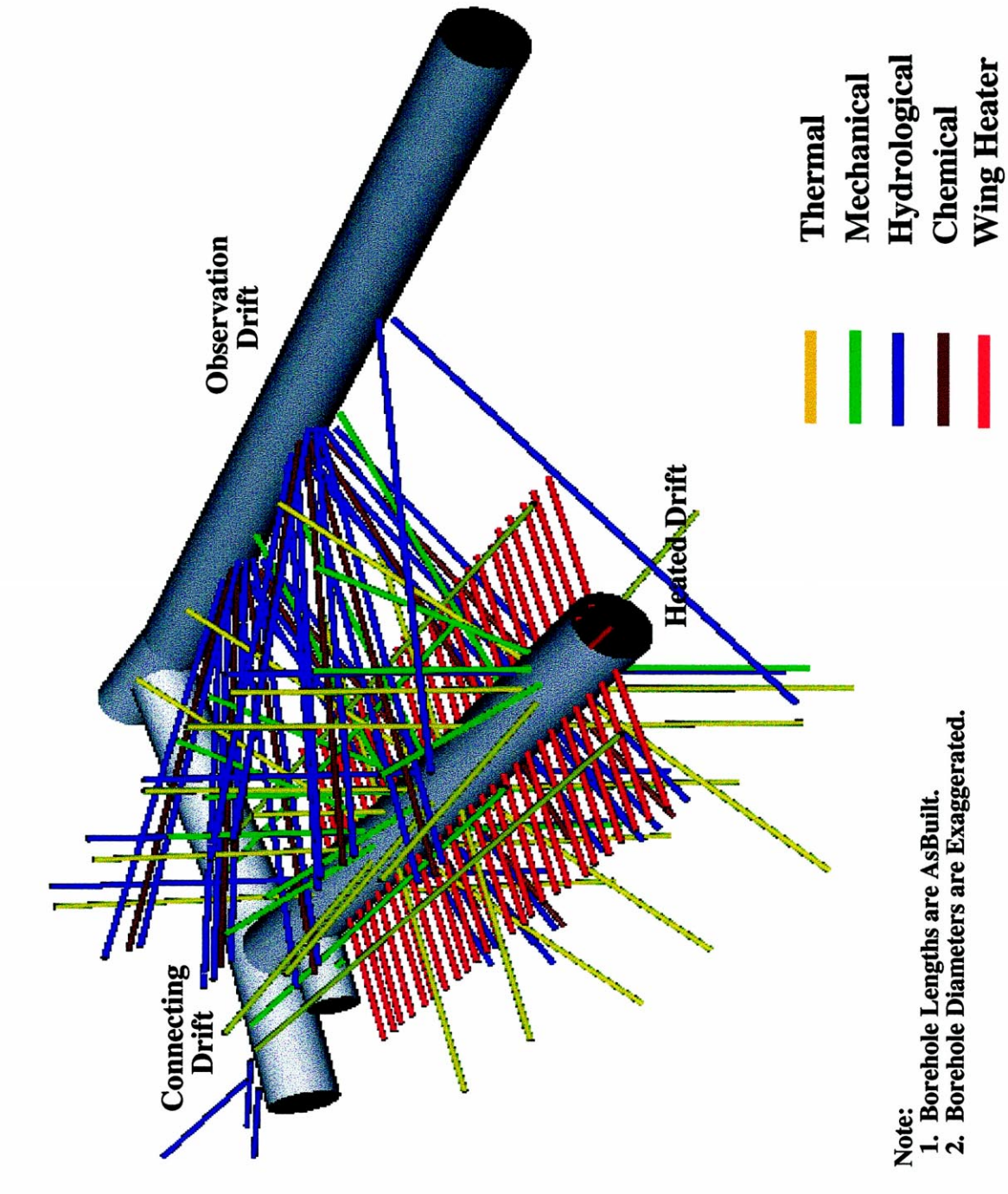

Fig. 2. (a) As-built 3-D perspective of boreholes in the Drift Scale Test. (b) As-built configuration of the nine canister and 50 wing heaters of the Drift Scale Test.

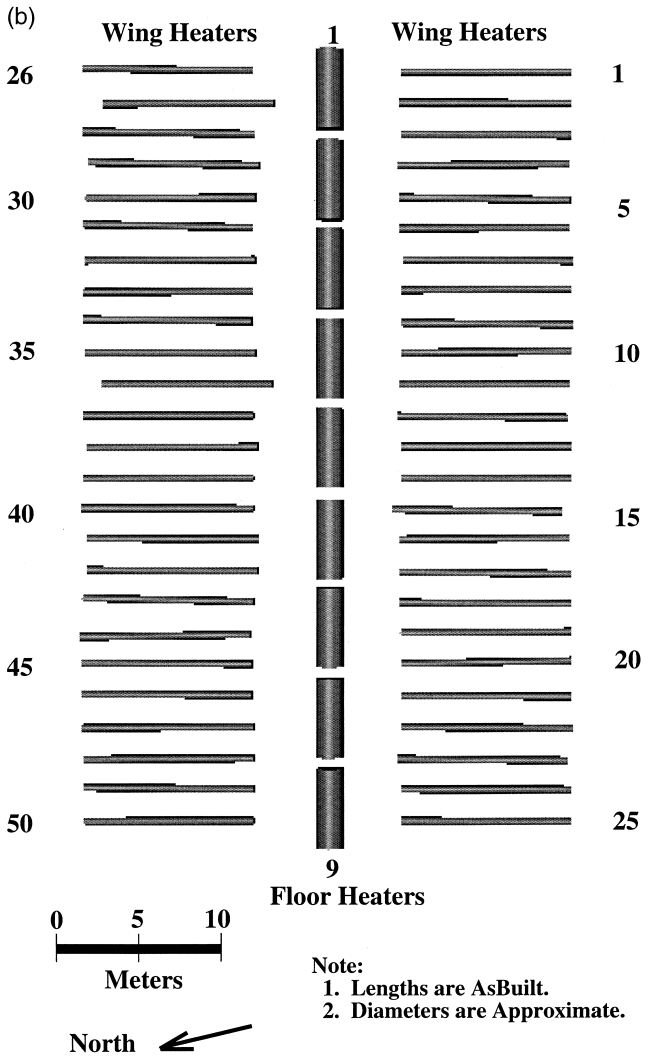

Fig. 2 (*continued*)

of small-scale heater tests conducted in the Underground Research Laboratory near Pinawa, Manitoba by the Canadian Nuclear Waste Program. In addition, large-scale thermal in situ tests have also been conducted at the Waste Isolation Pilot Plant (WIPP) in a salt formation in New Mexico, USA, as reported by Munson et al. [10,11]. These tests were conducted in long drifts to evaluate the thermal–mechanical response of the host rock to thermal loads that could result from the disposal of defense high level waste at the WIPP.

We note that the emphasis for most of the previously conducted tests was on thermal–mechanical processes, while the dominant coupled processes at Yucca Mountain relevant to repository performance is expected to be thermal–hydrological. A number of prototype tests in support of the Yucca Mountain Project have been conducted in welded and non-welded tuff (the same rock formation as that of the proposed repository) in the G-tunnel Underground Facility. While two of these prototype tests still dealt with the thermal–mechanical aspects as reported in Zimmerman et al. [12,13], a thermal–hydrological field test involving a 3-m-long single heater with power output of 1.1 kW/m was conducted for the duration of one year. The findings of Ramirez et al. [14] from this small-scale test were highly instructive and provided input for the design of the thermal tests discussed in this paper. The comparative increase in size, duration, and complexity of the SHT and DST, and the focus on all relevant thermal, hydrological, mechanical and chemical processes, is intended to provide much more in depth understanding of the performance of the proposed repository. The knowledge and benefits gained from these tests are anticipated to build con-

fidence in our ability to model the performance of the repository and to play an integral role in the licensing process for Yucca Mountain.

The Thermal Test Team, consisting of several organizations under the coordination of the Civilian Radioactive Waste Management System Management and Operating Contractor (CRWMS M&O) shares the scientific responsibility of fielding and interpreting the SHT and DST. All testing, data analysis, and numerical simulation of the thermal tests are largely carried out in three national laboratories: Sandia National Laboratories, Lawrence Livermore National Laboratory, and Ernest Orlando Lawrence Berkeley National Laboratory (Berkeley Laboratory). In this paper, we shall illustrate, by a few examples from the work performed by Berkeley Laboratory, how we arrive at a better understanding of the multi-phase thermal–hydrological response of the fractured rock mass to heat, through an iterative study involving both modeling and field measurements.

3. Measurements and modeling for probing the thermal–hydrological processes

The properties of the rock formation play a crucial role in dictating thermal–hydrological responses to heat. The middle nonlithophysal unit of the Topopah Spring welded tuff (in which the SHT and DST take place) has very low matrix permeability, on the order of microdarcies. On the other hand, the tuff is densely fractured, and the continuum permeability of the well-connected fractures is four to seven orders of magnitude larger than that of the welded matrix. Strong capillary forces hold a significant amount of water in the matrix pores — matrix liquid saturation is of the order of 90%, according to pre-test laboratory measurements of wet-drilled and wet-excavated samples from the thermal test blocks reported in Tsang et al. [15]. The fractures, if at thermodynamic equilibrium with the matrix at steady state, are essentially drained of water. So the flow of liquid and gas tend to move in different parts of the rock formation — liquid in the matrix, and gas in the fractures.

The anticipated response of the unsaturated fractured tuff to heat is the redistribution of moisture. As the formation temperatures approach 100°C around the heater(s), matrix pore water boils and vaporizes. Most of the vapor generated moves into the fractures, where it becomes highly mobile and is driven by the gas pressure gradient away from the heat source. When the vapor encounters cooler rock, it condenses, and the local saturation builds up. Part of the condensate may then be imbibed into the matrix, where it is subject to very strong capillary gradient towards the heat source, giving rise to a reflux of liquid to the drier areas around the heat source. Where there is a counter flow of vapor and liquid, two-phase conditions are maintained, giving rise to a "heat-pipe" signature in the temperature data (i.e., the temperature remains at the nominal boiling point). Because capillary forces are relatively weak in the fractures, we anticipate little liquid flow back to the drier area in the fractures resulting from capillary suction; rather, a substantial amount of condensate may drain by gravity.

It is clear from the above discussion that the dominant expression of thermal–hydrological coupled processes is the spatial distribution and time evolution of the drying and condensation zones. Therefore, in both the SHT and DST, neutron logging, electrical resistivity tomography, and cross-hole radar tomography are carried out in designated boreholes (labeled as "hydrological" in Figs 1 and 2), at appropriate intervals throughout the heater test, to probe the changes in the rock mass moisture content. Since most of the water resides in the matrix, changes of moisture content detected by the geophysical methods listed above reflect the changes in the rock matrix. On the other hand, since gas flow occurs predominantly in the fractures, interference air-permeability measurements in selected hydrological boreholes target the liquid-saturation changes in the fractures.

Modeling of the thermal–hydrological processes of the SHT and DST was carried out using the integral-finite-difference numerical simulator TOUGH2, developed by Pruess [16,17] for simulating multidimensional coupled transport of water, vapor, air, and heat in heterogeneous porous and fractured media. TOUGH2 accounts for the movement of gaseous and liquid phases (under pressure, viscous, and gravity forces according to Darcy's law, with interference between the phases represented by relative permeability functions), transport of latent and sensible heat, and phase transition between liquid and vapor. Mass- and energy-balance equations are written in integral form for an irregular flow domain in one, two, or three dimensions. The simulation includes the physical processes of capillary suction and adsorption in the liquid phase, binary diffusion in the gas phase, thermal expansion and porosity changes in the rock mass in response to pore pressure, and vapor pressure lowering as a result of capillary and phase adsorption effects. Furthermore, the numerical models also account for saturation dependence of the thermal conductivity.

For both the SHT and DST, the fractured welded tuff is conceptualized as a dual continuum, composed of the matrix continuum (with very low permeability) and the fracture continuum (with permeability orders of magnitude higher). As much as possible, we used site-specific data to assign appropriate material properties to the fracture and matrix continua. For example, thermal and hydrological properties for the tuff matrix

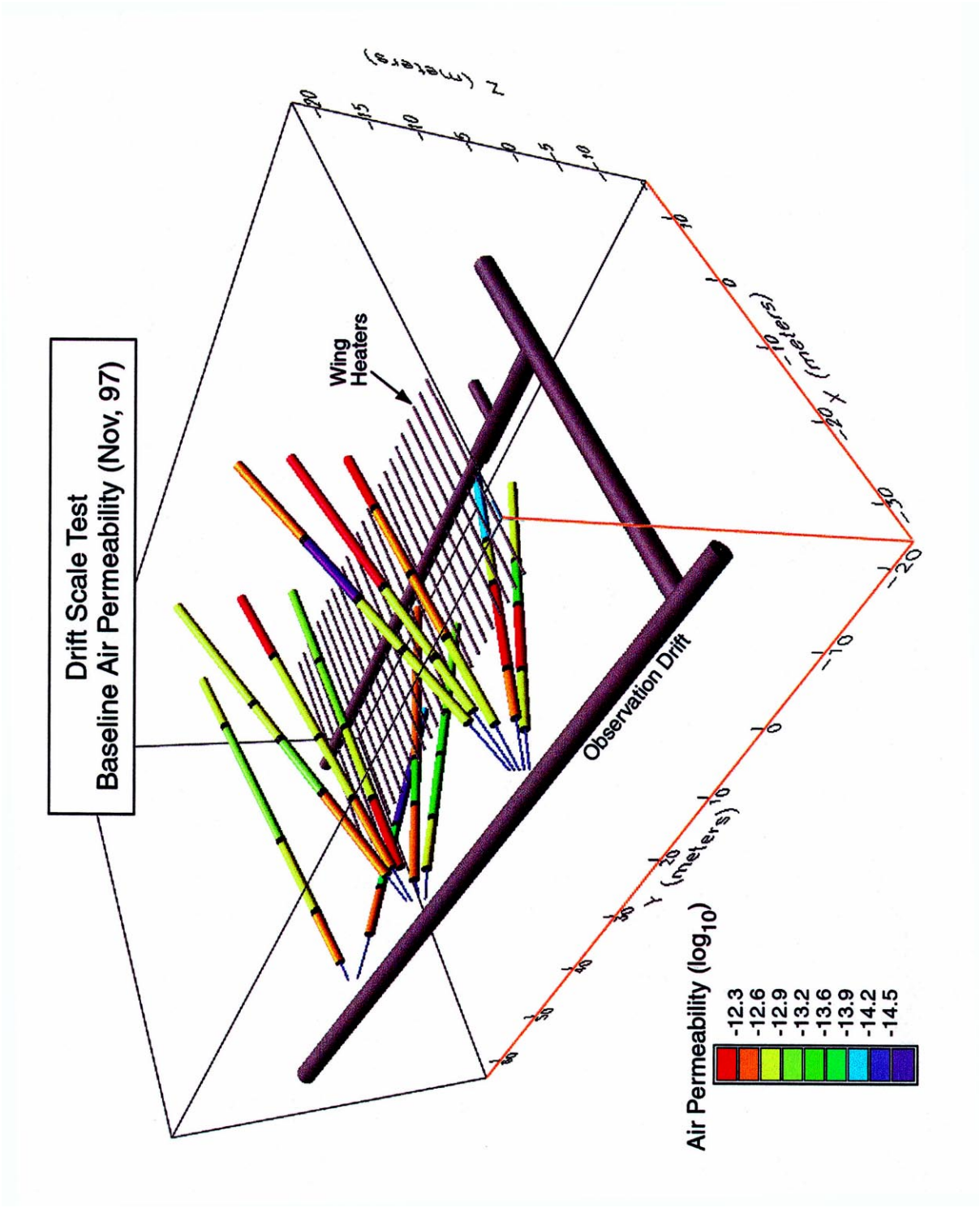

Fig. 3. Pre-heat baseline permeability measurements in zones isolated by packers in 12 40-m-long boreholes in the Drift Scale Test.

are supplied by the pre-test laboratory measurements on core samples from boreholes from the thermal test block and the fracture continuum permeability values from the pre-test field air-injection data. Where data specific to the thermal test block were not available, we employed measured parameter values for other locations in Yucca Mountain in the same stratigraphic units as the thermal tests.

Site specific 3-D models were constructed for SHT and DST, respectively. In each case, the computation domain for the thermal–hydrological simulations included the entire 3-D test block, plus significant rock volumes added in all directions to guarantee a proper definition of boundary conditions. The boundary conditions and the grids were designed to honor the 3-D test geometry including alcove and drifts, and to reflect the actual test conditions. A more detailed discussion of the numerical modeling of the SHT can be found in Birkholzer and Tsang [18] and Tsang and Birkholzer [19], and of the DST in Birkholzer and Tsang [20] and Chapter 2 of Tsang et al. [21].

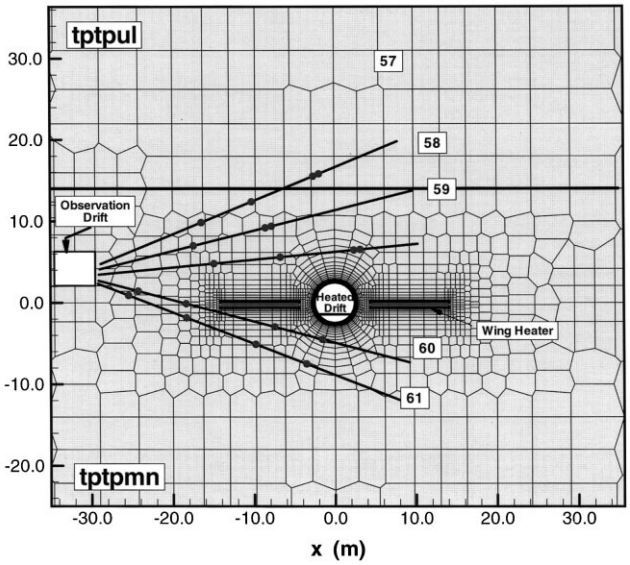

Fig. 4. A close-up view of numerical discretization in a 2-D vertical section (y = 10 m) containing one cluster of five hydrology holes (57 through 61) in the Drift Scale Test.

4. Key observation of thermal-hydrological processes in the thermal tests

4.1. Decrease in air-permeability in condensation zones in the Drift Scale Test

In this section, we illustrate how integrating modeling and measurements help to locate zones of increased fracture liquid saturation in the DST. These zones are identified by the change of air-permeability values with time. Fig. 3 shows the base line pre-heat air permeability measurements in the 12 (hydrological) holes that form three vertical fans — two fans of five holes each, with the third consisting of a pair of two boreholes. These three clusters are orthogonal to the Heated Drift, intersecting it at y = 10, 30, and 40 m from the bulkhead. The 40-m-long boreholes were installed with high-temperature inflatable packers to isolate each borehole into four[1] 8 to 10 m sections. Each isolated zone was equipped with air-injection line and pressure sensor. Air-permeability measurements were carried out in each of the 46 isolated zones in the 12 boreholes. A typical test consisted of air injection in one chosen zone at a constant flow rate maintained by mass flow controllers. Pressure responses in this and all other isolated zones were monitored continuously for about 60–90 min after steady state was reached, which was typically within minutes. Air injection was then terminated. The pressure response in the injection borehole was used to calculate the local permeability, averaged over the packed-off zone. Interference pressure responses in all other boreholes yielded information on the connectivity of pneumatic pathways between these observation zones and the injection zone.

The estimated permeability for different zones of the hydrology holes ranged over three orders of magnitude, from 1.6×10^{-15} to 9.7×10^{-13} m^2. The permeability is represented in a rainbow color palette in Fig. 3, with the highest value in red, and the lowest in blue. Interference pressure data indicate that pressure in all monitoring zones within ~10 m of the injection rise and fall with the injection, though the magnitude of the pressure response is only a fraction of that in the injection zone. These data indicate that on the scale of the DST, the fractures are well connected, forming a continuum as far as gas flow is concerned. Air-injection tests were and will continue to be conducted in these 12 boreholes periodically for the duration of the heating and cooling phases of the DST. In condensation zones, the resistance to airflow would increase during air-injection tests, resulting in a decrease in local permeability.

Numerical modeling of the DST predicts location and time evolution of condensation zones of increased liquid saturation. Fig. 4 shows a close-up view of a small xz vertical section of the numerical discretization for the DST 3-D numerical model. The small 2-D vertical section contains the first of three clusters of boreholes shown in Fig. 3 (i.e., boreholes 57 through 61). Note that the Observation Drift and the Heated Drift

[1] For two of the boreholes, boreholes 58 and 77, only three packers were installed due to numerous fractures and lithophysal cavities in the borehole walls.

are explicitly represented, and that the grids are extremely refined around the heaters where the temperature gradients are large. Fig. 5 shows the simulated fracture saturation at three, six and nine months of heating. Note the drying around the Heated Drift and the wing heaters, and the increase in fracture saturation due to condensation away from the heaters.

Figs. 4 and 5 identify locations of temperature sensors in these boreholes by circular markers, the sensor positions relate to those of the packers that isolated each borehole into air-injection zones. Different air-injection zones isolated by packers are represented by different colors denoting different permeability in Fig. 3. Zone 1 for each borehole is closest to the borehole collar between the first and second packers, and zone 4 is closest to the borehole bottom, between the fourth packer and the bottom of the borehole. For the two declining holes (60 and 61), locations of the packers coincide with that of temperature sensors marked in Figs. 4 and 5. For the upward-inclined boreholes (57, 58, 59), the third and fourth temperature sensors were installed at opposite ends of the fourth packer, while packer 1 is not identified with any temperature sensor shown on Fig. 4. Therefore, the end point of air-injection zone 1 for boreholes 57, 58, and 59 is defined by the first temperature sensor shown in Fig. 4, while the beginning of zone 1 is defined by the first packer near the collar shown not in Fig. 4, but only in Fig. 3.

It is evident from Fig. 5 that even at three months of heating, condensation build-up is apparent in zones 60-2, 60-3. As heating continues, zones of increased liquid saturation extend to 60-1 and 60-4, and to borehole 61 below the wing heater at six months of heating. Above the Heated Drift, borehole 59 and even borehole 58 begin to experience increased liquid saturation as heating continues to nine months of heating. Those air-injection zones in boreholes 57 through 61 that lie in locations of increased fracture liquid saturation would be expected to give lower air-permeability measurements.

Air-injection tests were carried out in March, April, June, and August of 1998; in other words, at approximately three, four, six and eight months after the first heating on 3 December 1997. Estimated permeability values were normalized to their pre-heat values (those shown in Fig. 3), and where there was more than a 10% decrease (the expected accuracy of our measurements), their values are displayed in Fig. 6. The horizontal axis of Fig. 6 is the date; the vertical axis shows the normalized permeability. It is evident that the zones that reside in condensation zones predicted by numerical simulations indeed display a decrease in air permeability. In particular, in zones 60-2 and 60-3,

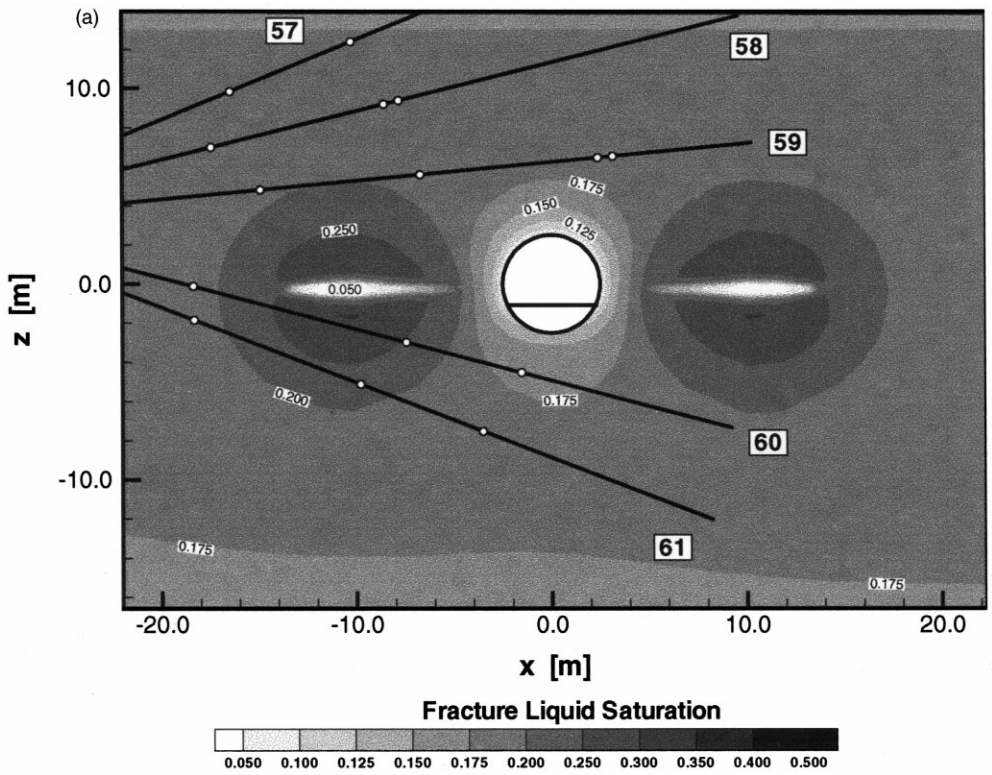

Fig. 5. Simulated fracture liquid saturation for boreholes 57 through 61 of the Drift Scale Test, at (a) three, (b) six and (c) nine months of heating.

there is a large decrease in permeability as early as at three to four months of heating, as predicted by the simulations in Fig. 5. In zone 2 of borehole 61, which is below borehole 60 and farther away from the heat source (wing heaters), data show a steady decrease in permeability as heating progresses. A similar trend of

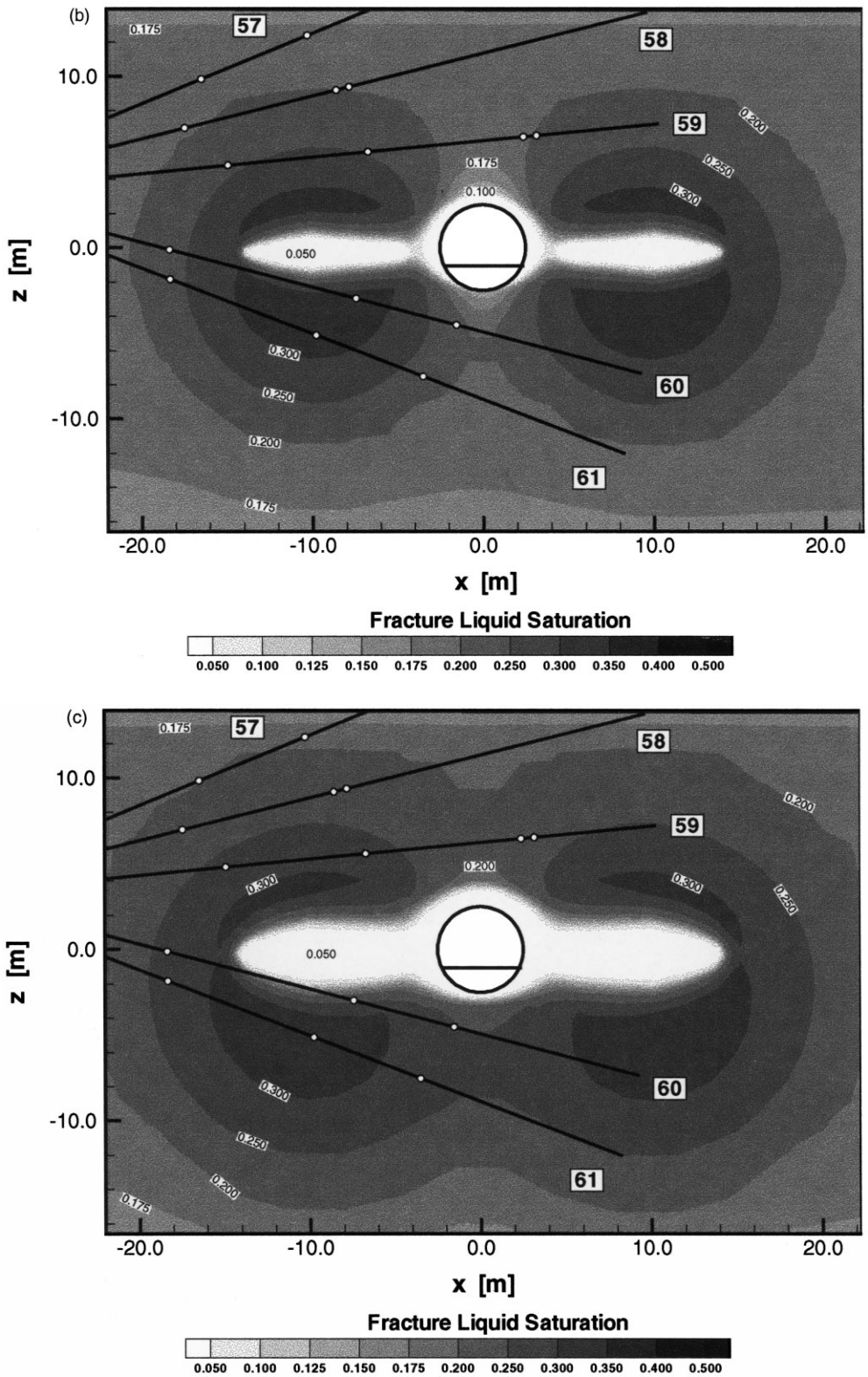

Fig. 5 (*continued*)

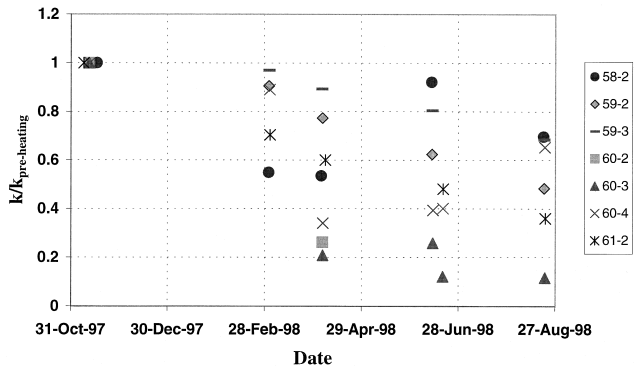

Fig. 6. Measured air-permeability (normalized to respective pre-heat values) for boreholes 57 through 61 for first nine months of heating of the Drift Scale Test.

steady reduction in permeability as liquid saturation builds up in time (from condensation of vapor) is seen in zones 2 and 3 of borehole 59, which is above the heater horizon.

The data in zones 60-4, however, show that the air permeability initially decreases significantly, then rises in August 1998, though still lower than their pre-heat values. Similarly, in zone 58-2, the permeability increases in the June measurements after an initial decrease in March and April, then drops in August. The fluctuation of permeability is not anticipated by the modeled results within this timeframe. Simulations (Fig. 5) predict that saturation in these zones should continue to build up (and therefore the permeability should continue to decrease) over nine months of heating. Our speculation is that the data in borehole sections 60-4 and 58-2 may be indicative of time-dependent gravity drainage, which is promoted by heterogeneities on a local scale arising from fractures. Our numerical model treats the fractures as a continuum and does not account for discrete fracture effects.

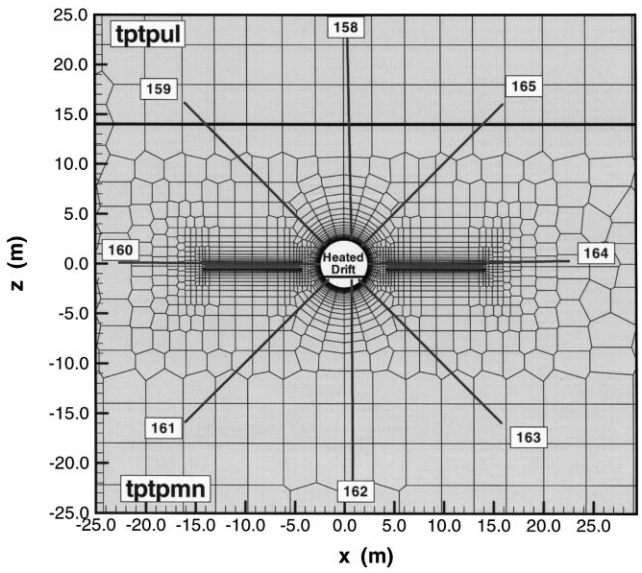

Fig. 7. A close-up view of model grids at $y = 23$ m for an array of boreholes (158 through 164) installed with temperature sensors at 0.3-m interval.

4.2. Heat-pipe signature in measured and simulated temperature data in the Drift Scale Test

Evidence of thermal-hydrological coupling can also be seen in temperature data. Fig. 7 shows a close-up view of model grids at $y = 23$ m for the array of temperature holes 158 through 164. In each of these 20-m-long boreholes, a string of temperature sensors were installed at 0.3 m intervals. In Fig. 8, we display the measured and simulated temperatures in selected sensors in borehole 160, which lies parallel to a wing heater. Sensor RTD-1 is closest to the Heated Drift wall at the collar of the borehole. Sensors RTD-17 and RTD-27

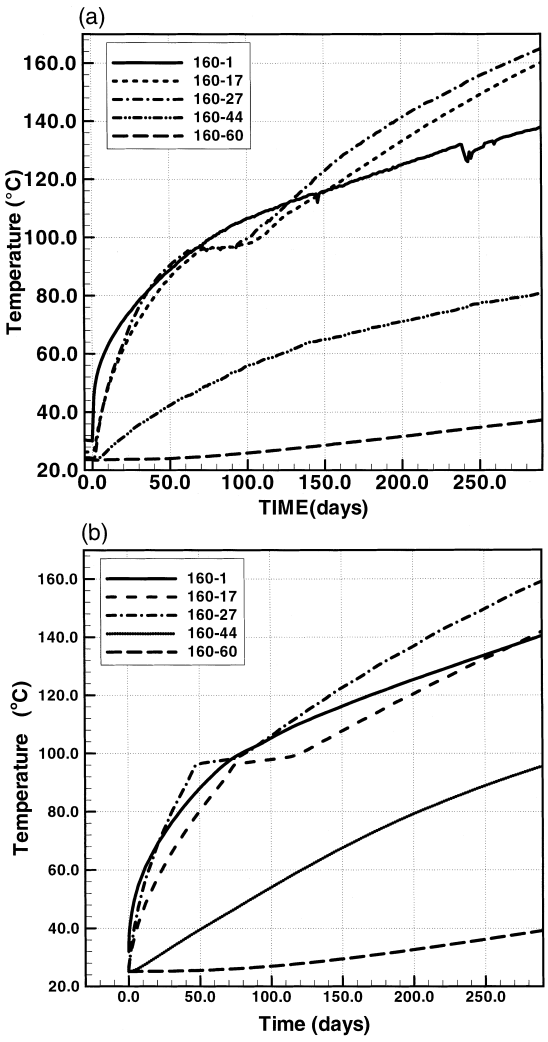

Fig. 8. Measured (top) and modeled (bottom) temperatures up to six months of heating for selected sensors in borehole 160 of the Drift Scale Test (day 0 refers to heater initiation date 2 December 1997).

have their x-coordinates within the range of the length of the wing heater, whereas sensors RTD-44 and RTD-60 are located toward the bottom of the borehole, and their x-coordinates are outside the range of the wing heater. The horizontal axis of Fig. 8 is the time line expressed in days since initiation of heat in the DST. At three months of heating, the temperature in RTD-1, the sensor closest to the Heated Drift, has already passed boiling, while those sensors near the bottom of the borehole, RTD-44 and RTD-60, are still very much below boiling at nine months of heating. Temperature data in sensors RTD-17 and RTD-27 clearly indicate a plateau at the nominal boiling point of 97°C from about 60–100 days after heating, indicating the presence of vapor and liquid counter flow and persistence of two-phase conditions. At about 100 days of heating, temperatures in these two sensors rise again; presumably the water around these sensors has boiled away, and heat conduction has taken over. Fig. 8 shows that the general thermal–hydrological response of these sensors is reproduced by the predictions from the numerical simulations in Chapter 2 of Tsang et al. [21].

4.3. Tracking fracture liquid saturation changes in the Single Heater Test

We also carried out air-injection tests in two boreholes in the SHT — during pre-heat, heating and cooling phases, and post-cooling — to monitor the thermal–hydrological coupled processes. (Readers are referred to Fig. 1 for the borehole layout of the SHT.) The boreholes are color-coded according to their function, as in the case of the DST. Note that those boreholes labeled "hydrological" originate either from the TMA Extension or the Observation Drift; they lie in a vertical plane orthogonal to the heater, intersecting the 5-m-long heater at its mid-point. Two pairs of boreholes that make the largest angle from the horizontal are for conducting electrical resistivity tomographic (ERT) measurements, while two pairs of boreholes that are closer to the heater horizon than the ERT holes are for neutron logging and for making cross-hole radar tomographic measurements. Both resistivity and radar measurements were carried out periodically throughout the heating and cooling phases of the SHT to monitor the liquid saturation changes in the rock matrix due to drying and condensation. The pair of hydrological boreholes (holes 16 and 18) that originate from the TMA Extension Drift, and that make the smallest angle with the heater horizon, are for periodic air-injection tests to target the changes in fracture liquid saturation.

Fig. 9 shows the simulated fracture liquid saturation contours (from a full 3-D numerical model of the SHT) at three and nine months of heating and three months of cooling, in the vertical plane of boreholes

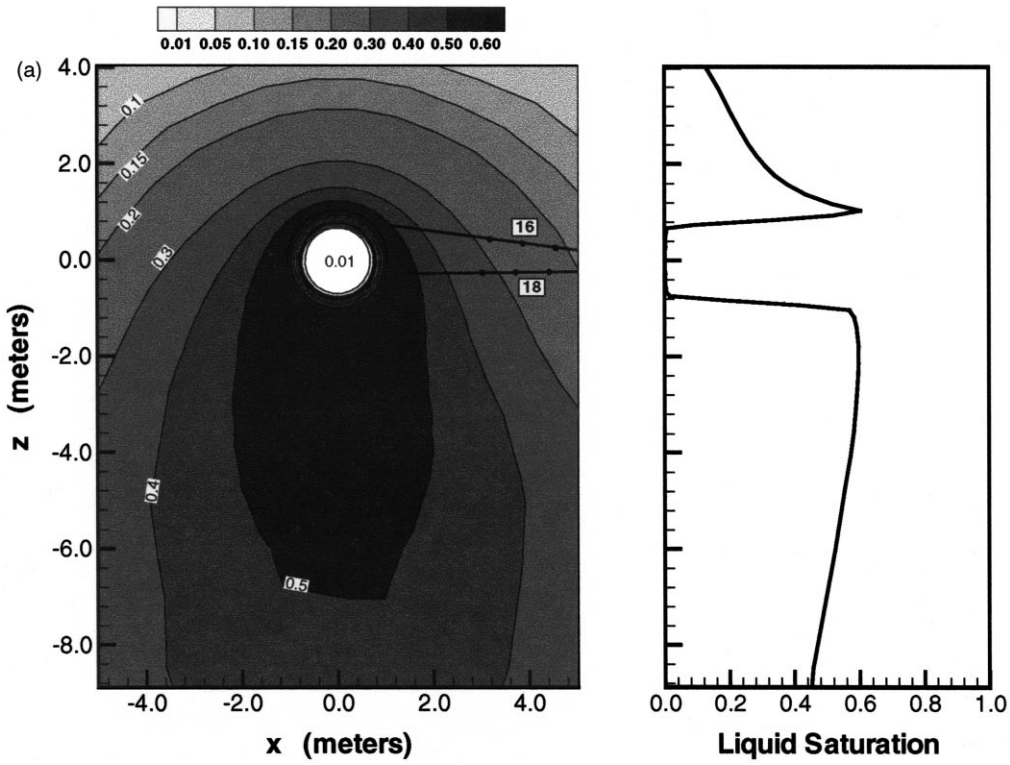

Fig. 9. Simulated fracture liquid saturation contours in a vertical 2-D cross section, intersecting the single heater at mid-plane (left graph) at (a) three and (b) nine months of heating, and (c) three months after cooling of the SHT. Right graph is the liquid saturation profile (vs elevation) at the center line of the heater.

16 and 18, orthogonal to the horizontal heater. These boreholes were installed with high-temperature inflatable packers, air-injection lines, and pressure sensors for air-permeability measurements. In addition, they were installed with temperature and relative humidity sensors that provided passive monitoring data on an

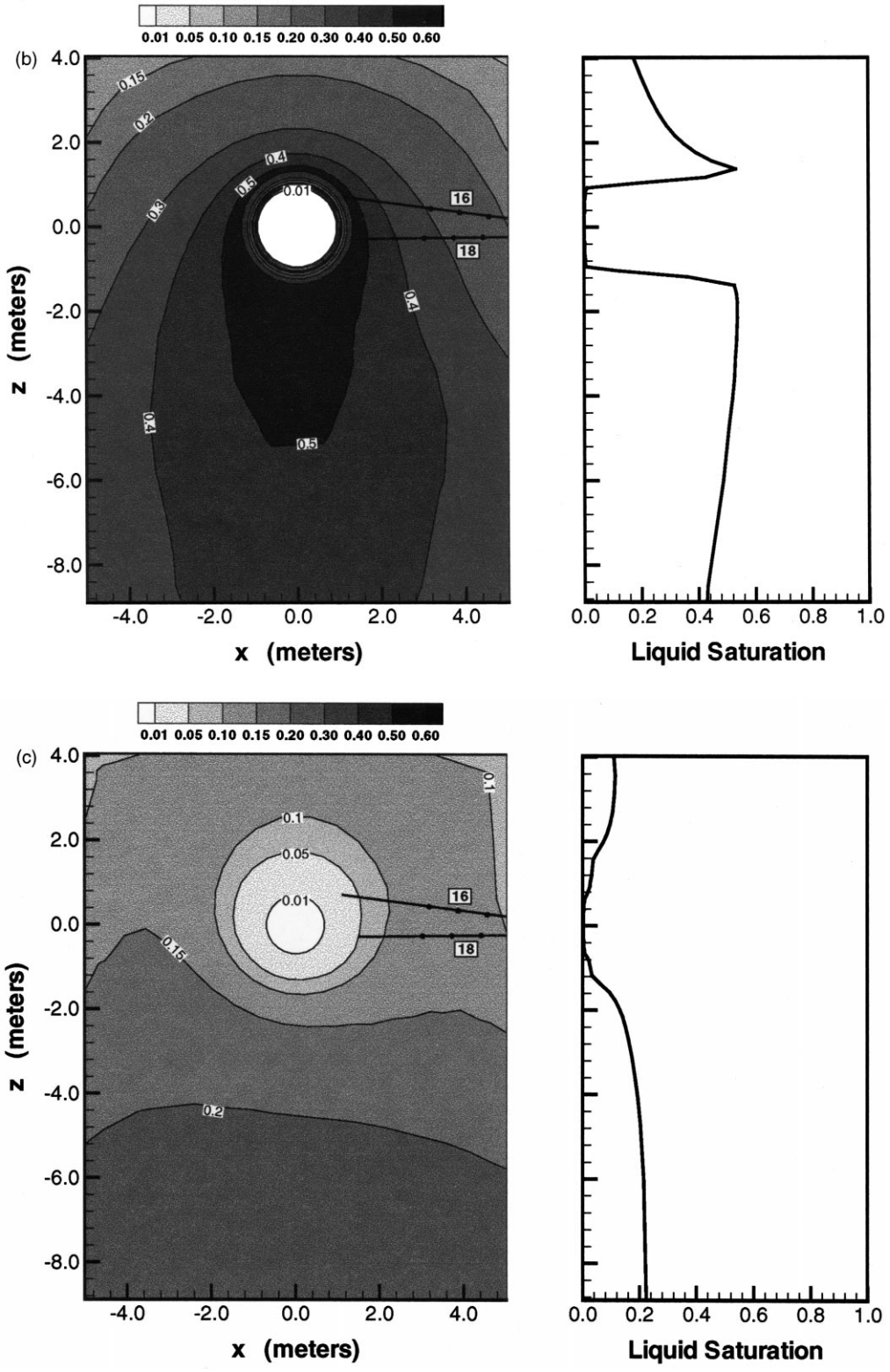

Fig. 9 (*continued*)

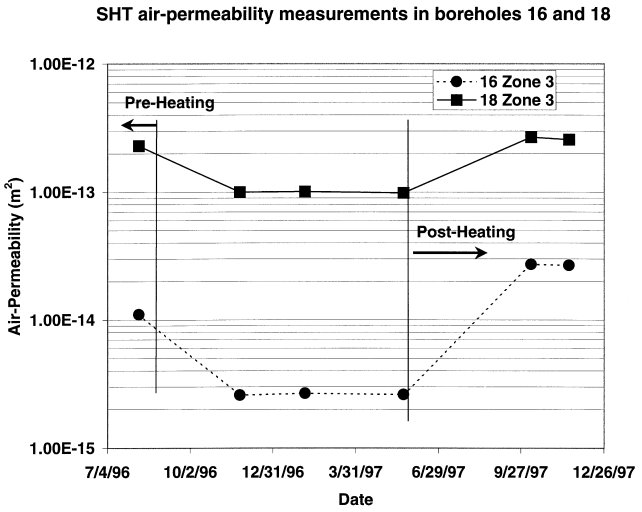

Fig. 10. Air permeability measurements in zone 3 of boreholes 16 and 18 for before, during, and after heating phase of the Single Heater Test.

hourly basis during the SHT. In Fig. 9, locations of three pressure sensors in each of the boreholes 16 and 18 are marked to define the zones where air-injection tests were conducted. (Zone 1 is that area between the first sensor (farthest from the heater) and the second sensor, zone 2 is that between the second and third sensors, and zone 3 is that between the third sensor and the bottom of the borehole closest to the heater.)

The liquid saturation contours in Fig. 9 show that at three months after heating, drying occurred around the heater, beyond which is an increase of liquid saturation from vapor condensation. Furthermore, the saturation contours also display significant gravity drainage in the fractures. Except for a larger drying region, the liquid saturation contours at nine months of heating are not significantly different from that at three months of heating. On the other hand, the contours at three months of cooling in Fig. 9 show that whatever saturation built up from condensation during heating has disappeared as a result of gravity drainage. Note that the region of increased fracture liquid saturation during heating coincides with zone 3 (for air-injection tests) of boreholes 16 and 18.

The air-permeability measurements, shown in Fig. 10, confirm the predictions of the 3-D numerical model for the SHT in Fig. 9. Specifically, in zone 3 of boreholes 16 and 18 where modeling results predict an increase in liquid saturation, resistance to airflow increases and air-permeability values decrease. (The horizontal axis of Fig. 10 is the time line with the heater activation and termination dates marked; the vertical axis is the air permeability.) Graphs in Fig. 10 show that a decrease of air permeability (from the pre-heat values) by a factor of four and two, respectively, for zone 3 of boreholes 16 and 18, during the entire heating phase of the SHT. The air permeability returns to its pre-heat values[2] after the termination of heating, which is consistent with the prediction of fracture liquid saturation at three months of cooling in Fig. 9. For zones 2 and 3 of holes 16 and 18, the air-permeability values remain at their pre-heat values throughout the test, attesting to no change in resistance to airflow. These measurements are also consistent with the predicted fracture liquid saturation contours from the numerical thermal–hydrological model (as shown in Fig. 9), which show little increase in liquid saturation in rock mass corresponding to these zones that are farther from the heater.

Not only did the air-permeability measurements confirm that zone 3 of 16 and 18 lie in locations of increased liquid saturation during the heating phase, but water was also found in zone 3 of borehole 16 and had been sampled before each air-permeability test for chemical and isotopic analysis. That water seepage into zone 3 of borehole 16 occurred indicates that build-up of condensate in rock mass in the vicinity of zone 3 of borehole 16 might have been rapid.

4.4. Matrix liquid saturation evolution in the Single Heater Test: predictions and measurements

The simulated matrix liquid saturation at three months and nine months after heating, and three months after cooling, are shown in Fig. 11. Fig. 11 shows a drying zone around the heater, and a condensation zone with liquid saturation higher than ambient values further from the heater, similar to those shown for the fracture saturation in Fig. 9 for the heating phase. Note that the drying zone extends from a radius of ~0.8 m around the heater after three months of heating, and ~1.2 m after nine months of heating. The increased matrix saturation below the heater horizon originates from gravity drainage in the fractures and subsequent imbibition into the matrix. At the termination of heating, the continuous process of vapor transport, condensation, and gravity drainage in the fracture ceased. The remaining dominant driving force for the movement of liquid in the matrix was that of capillary suction, which would move liquid from zones of higher liquid saturation back to the dry-out zone. A return of the matrix liquid saturation to its pre-test values due to capillary forces is a very slow process, hence in Fig. 11 the simulated liquid saturation continues to show a zone of increased saturation below the heater at three

[2] In fact, the post-heat permeability is slightly higher than the pre-heat values. Post-heat air permeability increase is found in other boreholes, which we hypothesize as indicative of thermally induced microfractures in [15].

months of cooling. We anticipate that the increased liquid saturation below the heater horizon will persist for a long time.

The extent of predicted drying and wetting zones from numerical modeling is consistent with the geophysical measurements: neutron logging, cross-hole radar and electrical resistivity tomography. Both neutron logging and cross-hole radar surveys were carried out in boreholes 15 and 17. Location of these boreholes are identified in Fig. 11 for the simulated matrix liquid saturation contours. Fig. 12 shows the tomograms derived from cross-hole ground penetrating

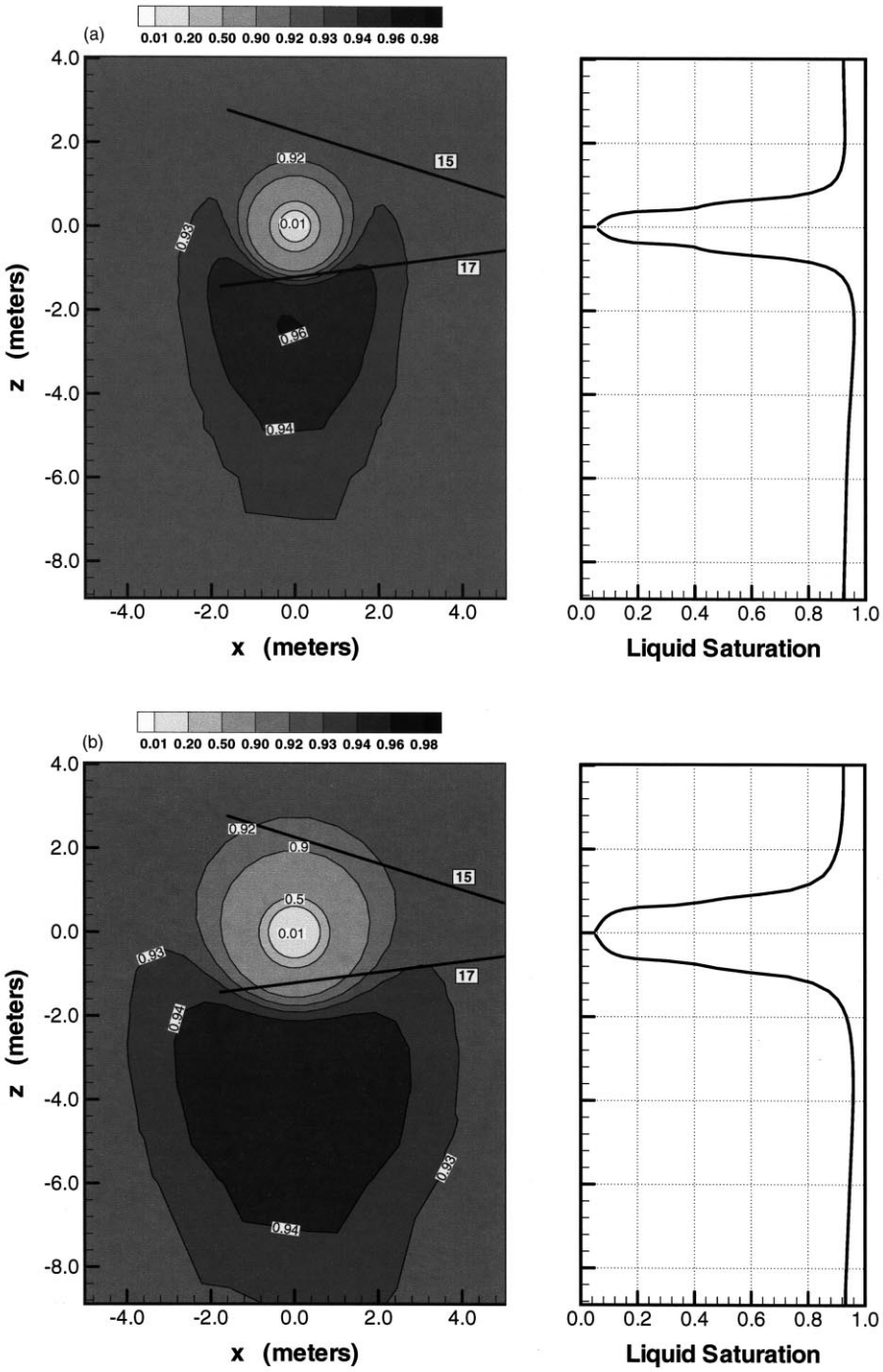

Fig. 11. Simulated matrix liquid saturation contours in a vertical 2-D cross section, intersecting the single heater at mid-plane (left graph) at three and nine months of heating; and three months after cooling of the Single Heater Test. Right graph is the liquid saturation profile (vs elevation) at the center line of the heater.

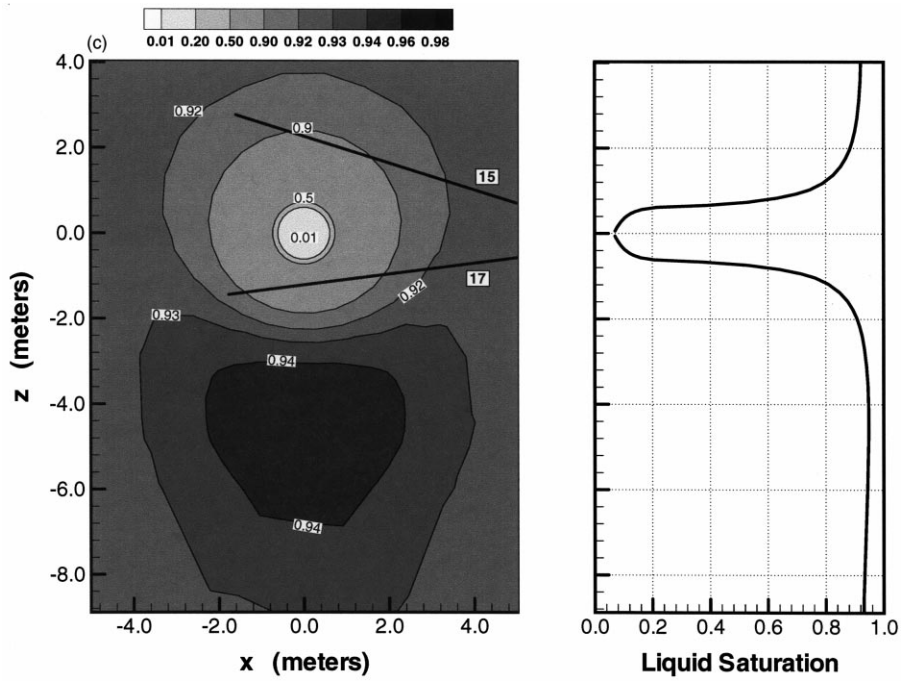

Fig. 11 (*continued*)

radar for the 2-D section between boreholes 15 and 17. Fig. 12 depicts the change in liquid saturation[3] from their pre-heat values during the heating and cooling phases of the SHT from the radar data. The change in liquid saturation is shown in a rainbow color palette, with red indicating drying from pre-heat conditions and blue indicating wetter than pre-heat conditions. Cross-hole radar velocity is inversely proportional to the square root of dielectric functions, which has both a temperature and liquid saturation dependence. The inversion of radar velocity to the saturation tomogram shown in Fig. 12 is based on a petrophysical model of the laboratory measurements of dielectric function by Roberts and Lin [22]. Note that the orientation of the tomograms are rotated 90° clockwise from that of Fig. 11, so that elevation in Fig. 12 is along the horizontal axis and borehole 15 (which is above the heater horizon) is to the right, while borehole 17 (below the heater horizon) is to the left. The heater horizon is at (0,0) marked by the black dot. Fig. 12 shows drying around the heater and condensation outside of the dry-out region. Note the increase in extent of drying from less than 1 m "radius" from the heater at five months of heating to more than 1 m at nine months, the end of the heating phase. The trend of an expanding drying region confirms the predictions in Fig. 11a and b. The slow process of rewetting discussed previously with respect to simulated results in Fig. 11c is corroborated by the tomogram at seven months after cooling in Fig. 12, where the drying around the heater persists. The tomograms also give a hint of less drying below rather than above the heater horizon. This asymmetry about the heater horizon is particularly noticeable in the tomogram for seven months after cooling. The higher matrix liquid saturation below heater horizon (attributed to gravity drainage in the fractures) was quite evident in the predicted results in Fig. 11. Moreover, it was also confirmed by laboratory measurements of liquid saturation from borehole cores drilled after the completion of the SHT cooling phase, as described in Tsang et al. [15] and Tsang and Birkholzer [19].

4.5. Condensate seepage into borehole 16 of the Single Heater Test indicative of discrete fracture phenomenon

In the previous sections, we have illustrated by several examples how the thermal-hydrological processes reveal themselves in measurements, the understanding of which is guided by results of realistic, 3-D numerical modeling. However, the modeling whose predictions show generally good agreement with the measured data conceptualize the densely spaced fractures as a continuum; that is, discrete fracture effects were not included in the elements of the conceptual and numerical models for the SHT and DST. The data, on the other hand, suggest effects of discrete fracture phenomena.

[3] The orientation of the tomogram is rotated 90° clockwise from that of Figs. 9 and 11.

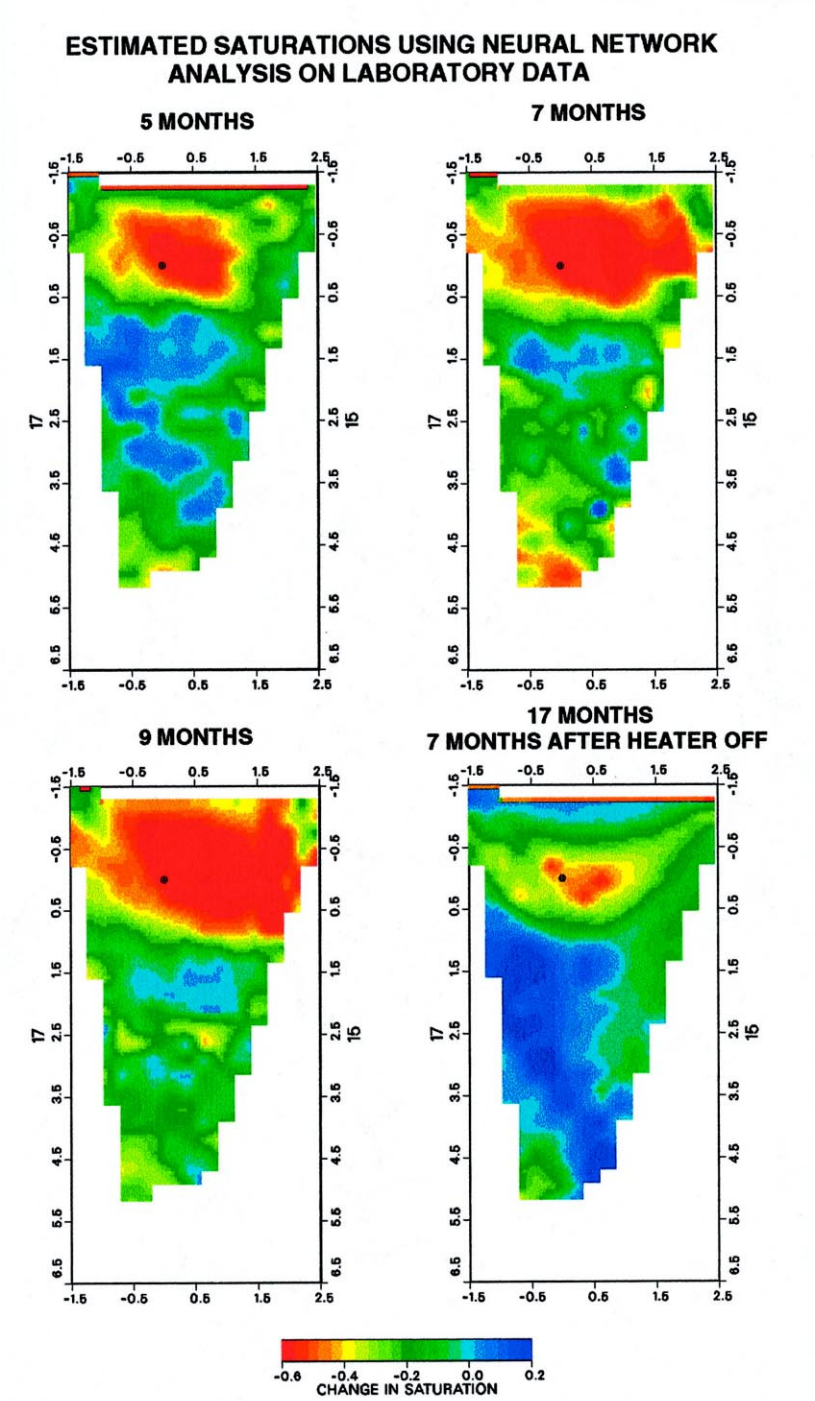

Fig. 12. Tomogram of liquid saturation changes (with reference to pre-heat values) derived from cross-hole ground penetrating radar surveys of borehole pair 15 and 17. Orientation of tomograms is rotated 90° clockwise from that of Fig. 11.

One example of this discrete fracture phenomenon is water seepage occurring in borehole 16 but not in borehole 18. Zone 3 of both boreholes 16 and 18 lies in zones of expected increased fracture saturation (Fig. 9), but water seepage occurred only in borehole 16, from which water samples were collected at four different times during the heating phase of the SHT. Not all borehole sections that lie in the predicted (from numerical simulations) condensation zones are expected to collect water because the borehole acts as a capillary barrier. Seepage into a borehole occurs only if the capillary barrier is overcome by the presence of fully saturated rock mass at the borehole wall. Localized zones of fully saturated rock mass at

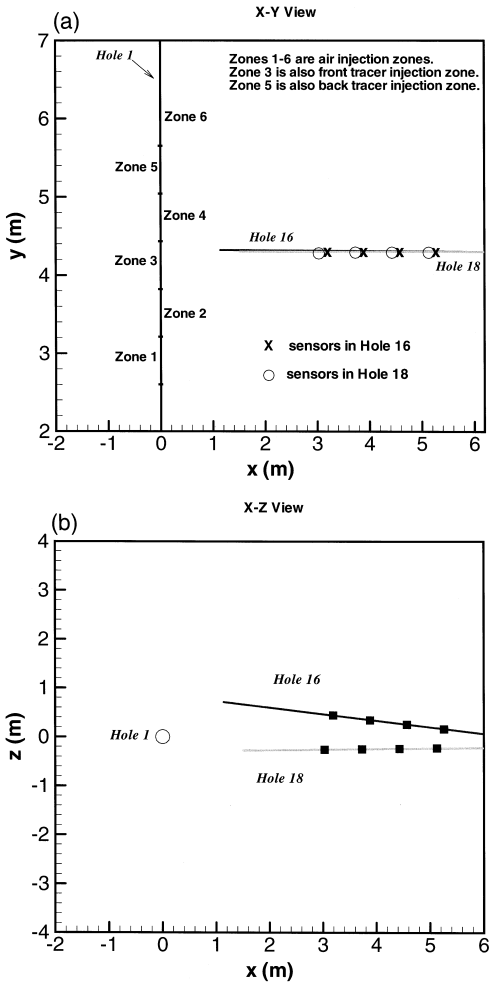

Fig. 13. Borehole configuration for interference air-injection tests and gas tracer tests.

the borehole wall could result from a fast path for vapor transport (for example, a fracture connection between the heater borehole 1, where vaporization takes place, and zone 3 of borehole 16, where condensation takes place). That water was found in borehole 16 and not in borehole 18 suggested that a fast path for vapor transport existed between heater borehole 1 and the former, but not the latter.

Post-cooling pneumatic characterization after the termination of the heating and cooling phases of the SHT allowed testing of this hypothesis. As part of this characterization, air-permeability tests were carried out in a multi-zone configuration for boreholes 1, 16, and 18. Specifically, we conducted injections in six consecutive zones in the heater borehole 1, and monitored the pressure response for zone 3 of boreholes 16 and 18. The multi-zone configuration for injection in borehole 1 and monitoring in boreholes 16 and 18 is shown in Fig. 13. Table 1 shows the cross-hole steady-state pressure response to the constant flux injection in isolated sections of borehole 1. The steady-state pressure change in the monitoring zones — zone 3 of boreholes 16 and 18 — are expressed as a fraction of the pressure response in the injection zone of borehole 1. It is clear that the strongest cross-hole response is between zone 3 of borehole 1 and zone 3 of borehole 16, with the second-strongest response from zone 5 of borehole 1 to zone 3 of borehole 18. Very weak cross-hole responses are obtained from injection in any other zones.

Upon conclusion of air permeability tests, we performed gas tracer tests between the heater borehole 1 and boreholes 16 and 18. Based on the results of the post-cooling air-permeability tests, zone 3 and zone 5 of borehole 1 were selected for gas injections. Pumping at boreholes 16 and 18 was at a rate 10 times higher than that of the gas tracer injection rate. The results of gas tracer tests showed that tracer transport from zone 3 of borehole 1 to zone 3 of borehole 16 was extremely rapid (first tracer breakthrough at 3 min), with 100% tracer mass recovery occurring within 30 min of injection. First arrival of tracer from the heater hole to zone 3 of borehole 18 took more than twice as long, and 100% tracer recovery took approximately 15 h. The differences in the transport times and recovery efficiencies suggests that the path between zone 3 of borehole 18 and borehole 1 is much more tortuous and indirect than the path between zone 3 of borehole 16 and borehole 1.

The post-cooling air-permeability and gas tracer tests therefore support the hypothesis that there exists a direct fracture connection between borehole 1 and zone 3 of borehole 16. Such a high-permeability connection does not exist in zone 3 of borehole 18, even though single-hole permeability analysis shows that

Table 1
Steady state pressure responses to constant flow rate air-injection in six consecutive zones in borehole 1

	1-Zone 1[a]	1-Zone 2	1-Zone 3	1-Zone 4	1-Zone 5	1-Zone 6
ΔP for injection in borehole 1	1.62	3.48	2.3	2.36	0.46	0.97
Permeability for zones in borehole 1	1.5e-13	6.8e-13	1.0e-12	1.0e-12	5.2e-12	1.4e-12
ΔP(16-zone 3)/ΔP(injection in 1)	1.54E-03	1.32E-02	3.54E-01	7.63E-02	1.02E-01	1.75E-02
ΔP(18-zone 3)/ΔP(injection in 1)	1.54E-03	8.19E-03	2.39E-02	2.12E-02	2.35E-01	2.89E-02

[a] Injection flowrate is 1 SLPM for Zone 1, 10 SLPM for Zones 2–6.

zone 3 of borehole 18 has a higher air-permeability than zone 3 of borehole 16 (Fig. 10). Hence the data during heating and cooling suggested discrete fracture phenomenon, and the post-cooling characterization data confirmed the presence and location of the fracture. It is unlikely that the presence of these discrete and the exact thermal-hydrological responses of the rock mass can be predictable a priori. Although the numerical simulations can predict zones of increased liquid saturation that agree with measurements, it is not likely that the exact location of water seepage can be foreseen. The uncertainty is entirely with the geometry of the fractures, which play little role in affecting the thermal response of the rock mass. That is, the temperature predicted from our numerical model (which conceptualize the fractures as a continuum) matches extremely well with those measured, as reported in Tsang and Birkholzer [19].

5. Conclusion

Understanding multiple processes in a complex geological setting of partially saturated fractured rock is a challenge. In the two large-scale thermal tests at Yucca Mountain, we have used an iterative approach requiring close integration between measurements and modeling, making significant progress. In this paper, I have presented the identification and study of a number of key features of these thermal-hydrological processes. The main manifestation of coupled thermal-hydrological processes is in the time evolution of the drying and condensation zones. Good agreement occurred between the model predictions and measurements; specifically on the decrease in air-permeability values for zones of increased liquid saturation in the fractures and the increase of radar velocity (from cross-hole radar surveys) for zones of decreased liquid saturation in the rock matrix. Heat-pipe signature in the temperature data — a small temperature gradient and constant temperature readings at the nominal boiling point — indicating two-phase regions of liquid-vapor counterflow is seen in both the measurements and simulated results for the DST. The general agreement between predictions from the numerical simulations and the measurements in the thermal tests indicates that our fundamental understanding of the coupled thermal–hydrologic processes at Yucca Mountain is sound. However, detailed behavior is impacted by site-specific heterogeneity, in the form of discrete fractures that are not likely to be predictable a priori. One emphasis of the on-going DST is to build on the present understanding and to assess the impact of heterogeneity on the performance of the repository.

Acknowledgements

We thank Chin-Fu Tsang and Dan Hawkes of LBNL for their review of the manuscript and comments for improvement. The success of the completed SHT and the progress of the DST are a direct result of the multi-laboratory teamwork of the Thermal Test Team. I would especially like to acknowledge Robin Datta of Woodward Clyde Federal Services, the coordinator of the Thermal Test Team; Douglas Weaver of Los Alamos National Laboratory, the project engineer; and Fred Homuth of Los Alamos National Laboratory, the data manager. As for my colleagues at Berkeley, I am grateful to Jens Birkholzer for his indispensable role in the numerical modeling of the SHT and DST, Barry Freifeld for his contribution to the air permeability and gas tracer field testing, and Ken Williams and John Peterson for collection and analysis of the radar data. This work was supported by the Director, Office of Civilian Radioactive Waste Management, US Department of Energy, through Memorandum Purchase Order EA9013MC5X between TRW Environmental Safety Systems and the Ernest Orlando Lawrence Berkeley National Laboratory (Berkeley Laboratory). The support is provided to Berkeley Laboratory through the US Department of Energy Contract No. DE-AC03-76SF00098.

References

[1] CRWMS M&O Characterization of the ESF Thermal Test Area. Report B00000000-01717-5705-00047, TRW Environmental Safety Systems Inc., Las Vegas, Nevada, 1996.
[2] CRWMS M&O Ambient characterization of the Drift Scale Test block. Report BADD0000-01717-5705-0001 REV 01, TRW Environmental Safety Systems Inc., Las Vegas, Nevada, 1997.
[3] Cook NGW, Hood M. Full scale and time-scale heater experiments at Stripa: preliminary results. Technical Report LBL-7072, Lawrence Berkeley National Laboratory, Berkeley, CA, 1978.
[4] Cook NGW, Witherspoon PA. Mechanical and thermal design considerations for radioactive waster repositories in hard rock. Parts I and II. Technical Report LBL-7072 Lawrence Berkeley National Laboratory, Berkeley, CA, 1978.
[5] Chan T, Cook NGW. Calculated thermally induced displacements and stresses for heater experiments at Stripa, Sweden. Linear thermoelastic models using constant material properties. Technical Report LBL-7061, SAC-22, Lawrence Berkeley National Laboratory, Berkeley, CA, 1979.
[6] Witherspoon PA, Cook NGW, Gale JE. Progress with field investigations at Stripa. Technical Report LBL-10559, Lawrence Berkeley National Laboratory, Berkeley, CA, 1980.
[7] Dubois AO, Hood M, Binnall EP, Anderson L. Extensometer performance during heater experiments at Stripa; Swedish–American cooperative program on radioactive waste storage in mine caverns in crystalline rock. Technical Report LBL-13531, SAC-50, UC-70, Lawrence Berkeley National Laboratory, Berkeley, CA, 1981.
[8] Gregory EC, Kim K. Preliminary results from the full-scale heater tests at the near-surface test facility. In: Proceedings of the

22nd US Rock Mechanics Symposium, Massachusetts Institute of Technology, Cambridge, MA, 1981 July.

[9] Matino JB, Read RS. Mine-by-experiment phase III-heater failure tests. Technical Progress Report and Summary of State I. Atomic Energy of Canada (AECL) Report TR-652, COG-94-478, URL-EXP-022-R32, Whiteshell Laboratories, Pinawa, Canada, 1994.

[10] Munson DE, Jones RL, Ball JR, Clancy RM, Hoag DL, Petney SV. Overtest for simulated defense high-level waste (Room B). In situ data report (May 1984–February 1988) Waste Isolation Pilot Plant (WIPP) Thermal/Structural Interactions Program. Technical Report SAND89-2671, Sandia National Laboratories, Albuquerque, New Mexico, 1990.

[11] Munson DE, Petney SV, Christian-Freir TL, Ball JR, Jones RL, Northrop-Salazar CL. 18 W/m^2 Mockup for defense high level waste (Room A): In situ data report Vol II — thermal response gages (February 1985–June 1990). Technical Report SAND90-2749, Sandia National Laboratories, Albuquerque, New Mexico, 1992.

[12] Zimmerman RM, Blanford ML, Holland JF, Schuch RL. Final Report: G-Tunnel Small Diameter Heater Experiments. Technical Report SAND84-2621, Sandia National Laboratories, Albuquerque, New Mexico, 1987.

[13] Zimmerman RM, Schuch RL, Mason DS, Wilson ML. Final Report: G-Tunnel Heated Block Experiment. Technical Report SAND84-2620, Sandia National Laboratories, Albuquerque, New Mexico, 1986.

[14] Ramirez AL, Buscheck T, Carlson R, Daily W, Lee K, Lin W, Mao N-H, Ueng H, Wang T-S, Watwood D. Prototype Engineering Barrier System Field Tests (PEBSF) Final Report. Technical Report UCRL-ID-106159, Lawrence Livermore National Laboratory, Livermore, CA, 1991.

[15] Tsang YW, Apps J, Birkholzer JT, Freifeld B, Hu MQ, Peterson J, Sonnenthal E, Spycher N. Yucca Mountain Single Heater Test final report. Technical Report LBNL-42537, Lawrence Berkeley National Laboratory, Berkeley, CA, 1999a.

[16] Pruess K. TOUGH user's guide. Technical Report LBL-20700, Lawrence Berkeley National Laboratory, Berkeley, CA, 1987.

[17] Pruess K. TOUGH2 — A general purpose numerical simulator for multiphase fluid and heat flow. Technical Report LNL-29400, UC-251, Lawrence Berkeley National Laboratory, Berkeley, CA, 1991.

[18] Birkholzer JT, Tsang YW. Forecast of thermal-hydrological conditions and air-injection test results of the Single Heater Test at Yucca Mountain. Technical Report LBNL-38789, Lawrence Berkeley National Laboratory, Berkeley, CA, 1996.

[19] Tsang YW, Birkholzer JT. Predictions and observations of the thermal-hydrological conditions in the Single Heater Test. Journal of Contaminant Hydrology 1999;38(1–3):385–425.

[20] Birkholzer JT, Tsang YW. Pretest analysis of the thermal-hydrological conditions of the Drift Scale Test at Yucca Mountain. Technical Report LBNL-41044, Lawrence Berkeley National Laboratory, Berkeley, CA, 1997.

[21] Tsang YW, Apps J, Birkholzer JT, Peterson J, Sonnenthal E, Spycher N, Williams K. Yucca Mountain Drift Scale Test progress report. Technical Report LBNL-42538, Lawrence Berkeley National Laboratory, Berkeley, CA, 1999b.

[22] Robert JJ, Lin W. Electrical properties of partially saturated Topopah Spring Tuff: water distribution as a function of saturation. Water Resources Research 1997;33(4):577.